Fabric liquid diode for electricity generation and self-cooling

Renbo Zhu [a,b], *Zhongliang Zhang* [a,b], *Kitming Ma* [a,b], *Yonghui Luo* [a,b], *Jing Yang* [a,b], *Su Liu* [a,b], *and Xiaoming Tao* [a,b,]*

[a] Research Institute for Intelligent Wearable Systems, The Hong Kong Polytechnic University, Hong Kong 999077, China.

[b] School of Fashion and Textiles, The Hong Kong Polytechnic University, Hong Kong 999077, China.

E-mail: xiao-ming.tao@polyu.edu.hk

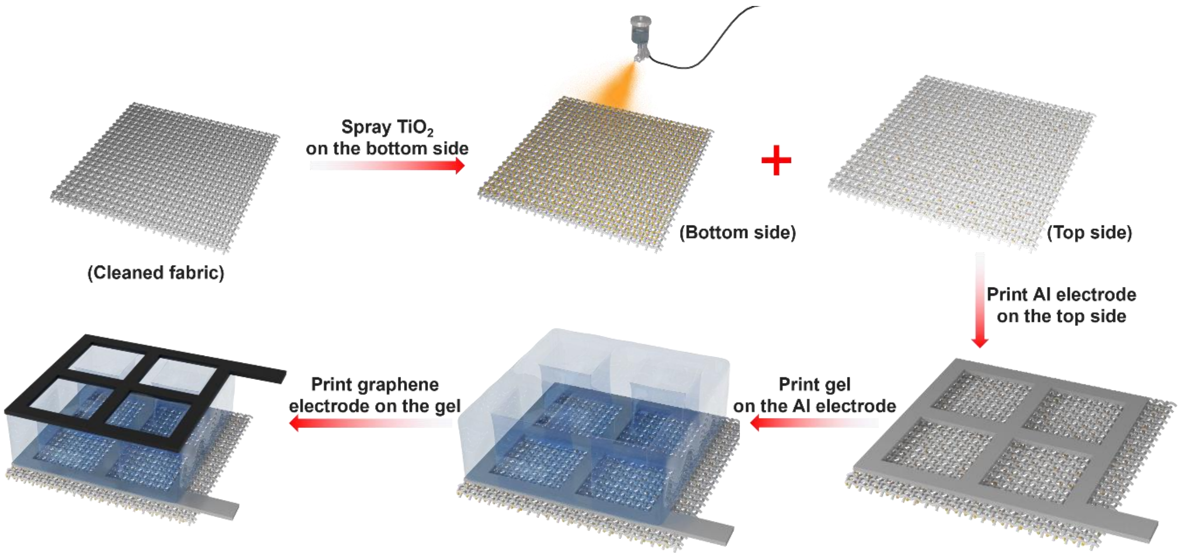

Supplementary Fig. 1 Fabrication process illustration of self-powered and self-cooling fabric.

Supplementary Table 1 Summarization of recent hygroelectric generators with water evaporation.

Materials	RH (%)	I_{max} (μA·cm^{-2})	V_{max} (V)	P_{max} (μW·cm^{-2})	Moisture management	Ref.
Carbon black	66	0.06	1	0.02	No	1
P(VdF-HFP)	70	306	0.88	51	No	2
PSS/PVA	100	1.7	1	0.1	No	3
Mac-fabric	40	128	0.85	0.01	No	4
$Ti_3C_2T_x$/PAM	20	15	0.6	24.8	No	5
Cellulon paper	60	0.83	0.78	0.7	No	6
PSSA/PDDA	25	0.2	0.95	0.076	No	7
Bilayer polyelectrolyte	80	11.67	1.1	2.6	No	8
Si nanowires	45	55	0.4	6	No	9
Microbial biofilms	50	7	0.5	2.8	No	10
SSF	55	400	0.86	77.5	Yes	This work

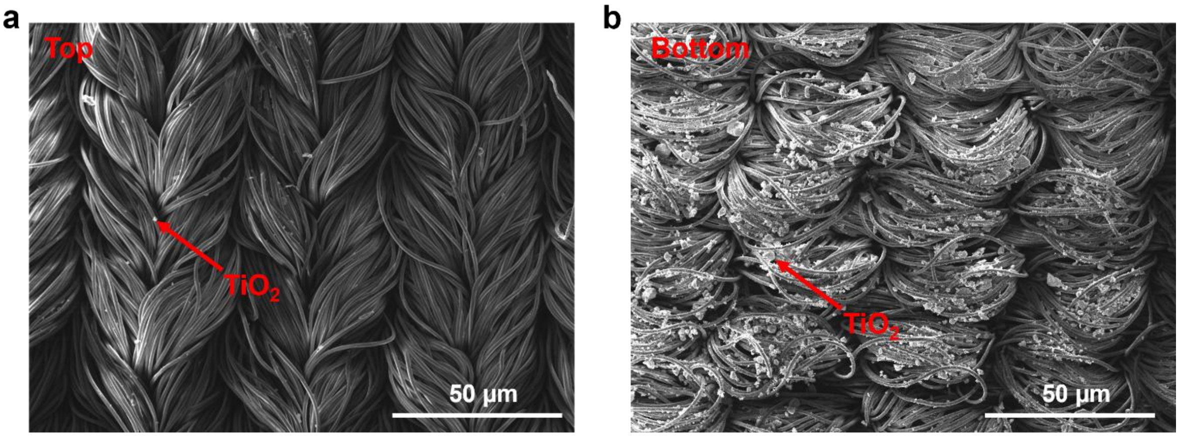

Supplementary Fig. 2 The morphology of fabric liquid diode from SEM images. a, Top side. **b**, Bottom side.

Supplementary Table 2 Element distribution on the different surface of fabrics by XPS.

	Si (%)	C (%)	N (%)	Ti (%)	O (%)
Nylon	6.75	69.65	6.75	0	16.85
“I”	9.55	35.67	2.18	10.4	42.19
“O”	5.38	21.29	2.76	20.51	50.06

Supplementary Note 1.

Energy calculation in the water evaporation: The calculation of energy conversion was also investigated. The SSF absorbs energy from skin surface and environment to achieve water evaporation. The energy driving water evaporation is calculated by molar phase transition heat formula:

$$q = \Delta H_v \cdot m \tag{4}$$

Where ΔH_v is latent heat of water evaporation, m is mass of water evaporation. ΔH_v and m for each operation is 2444 $J \cdot g^{-1}$ and 0.2 g, respectively. The energy from water evaporation is 488.9 J for one operation cycle.

In the electricity generation, SSF was discharged with an external load of 2 kΩ. The electric power is calculated as follows:

$$W = R \int I^2 dt \tag{5}$$

Where R and I are the external resistance and current output, respectively. W is 0.42 J with an external load of 2 kΩ.

The SSF device achieves self-cooling in the water evaporation. The cooling capacity of SSF devices is calculated according to the sensible heat formula as follows:

$$Q = \sum m_i \cdot c_i \cdot \Delta T \tag{6}$$

Where m_i and c_i are the mass and specific heat capacity of different composites. ΔT is the temperature change of SSF devices. The cooling capacity of SSF is 7.6 J for one operation cycle.

Supplementary Note 2.

Water contact angle and breakthrough pressure: In the water contact angle test of fabrics with different TiO_2 ratios (Supplementary Fig. 3), water passes through hydrophilic side in 1 s and spreads on the hydrophilic side, which contributes to the no obvious water contact angle (blue curve) when water was dropped on the hydrophilic side. By dropping water on the hydrophobic side, water passes through the hydrophobic side slowly when TiO_2 ratio is less than 4% (yellow curve). The water contact angle was recorded in 1 s after water was dropped. Water was blocked by the hydrophobic side when TiO_2 ratio is higher than 4% as excess TiO_2 particles filled the water transport channels in the fabrics.

To measure the breakthrough pressure, the one side of fabric was covered with a hollow cylinder and blocks water with a certain height from a pump (Supplementary Fig. 4). The contact areas of fabric and cylinder was connected and sealed by the tape. The cylinder was filling with water at a rate of 0.05 $mm \cdot s^{-1}$ until water passed through the fabric. The maximum height of water in the cylinder was denoted as breakthrough pressure.

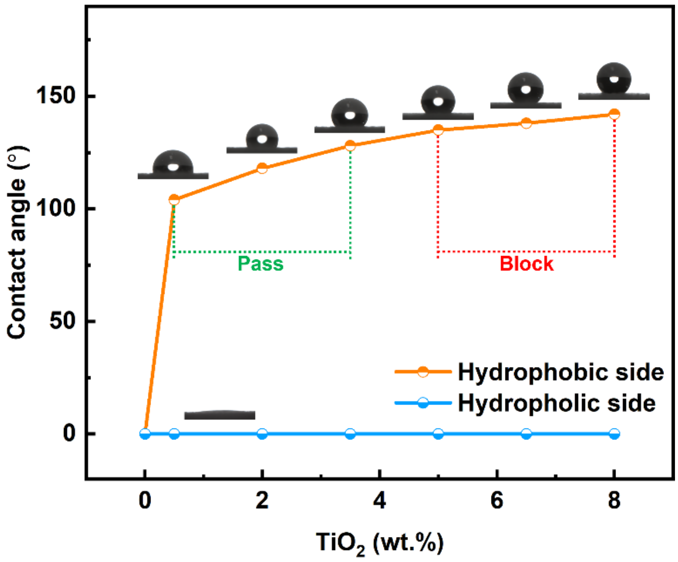

Supplementary Fig. 3 The water contact angle of hydrophilic and hydrophobic sides of liquid diode fabricated with different TiO_2 contents. The shape of water droplet was recorded in 1 s after water came into contact with fabric.

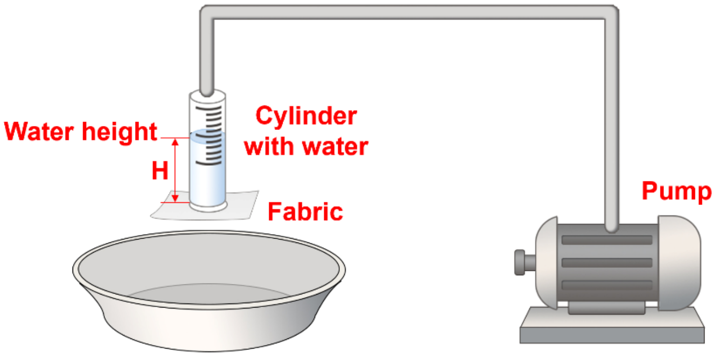

Supplementary Fig. 4 Schematical illustration of breakthrough pressure test.

Supplementary Note 3.

Mechanism analysis of water transport: In the directional water transport in the liquid diode (Supplementary Fig. 5), water contact angle (θ) was used to analyse the hydrophilicity of water transport channel and interaction between water and channel surface. Expansion/contraction angle (α) is related to the expansion or contraction of water transport channel, which is close to -90° or 90° in a sharp contraction or expansion along the water transport path. The water flow will pass through channels according to the Gibbs pinning criterion[11] when θ and α are designed as follows:

$$\theta + \alpha < 90° \tag{2}$$

Water flow will be blocked when $\theta + \alpha$ is higher than 90°. The driving force of water transport origins from the capillary pressure as follows:

$$C = \frac{\alpha\gamma \sin\left(\theta + \alpha - \frac{\pi}{2}\right)}{L} \tag{3}$$

Where C, γ and L represent capillary pressure, surface tension and half-width distance of channels. When $\theta + \alpha < 90°$, the calculated capillary pressure is lower than 0, which indicates that water flow pass through the channels without transport barrier. Conversely, the positive capillary pressure ($\theta + \alpha > 90°$) contributes to the transport barrier of water flow, which blocks water flows with a height lower than the capillary pressure. When the height of water flow exceeds the capillary pressure, water will pass through SSF.

In the direction "I", water transported from one side ($\theta + \alpha < 90°$) and was blocked by the other side ($\theta + \alpha > 90°$). In the direction "II", water transported inside the channels ($\theta + \alpha < 90°$) under the one-way driving force due to the elaborated water contact angle and expansion/contraction angle.

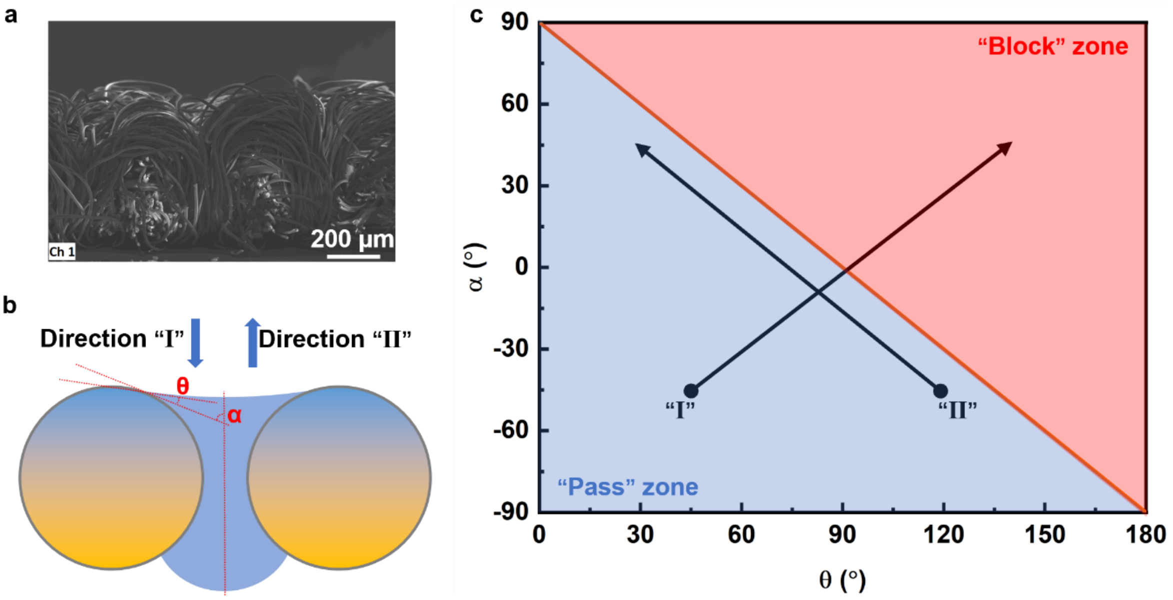

Supplementary Fig. 5 Water transport in the gradient channel. a, The cross-section morphology of nylon fabric from SEM images. **b**, Schematical illustration of water transport with expansion/contraction angle of α and water contact angle of θ in different directions. **c**, The water transport in different directions with varied α and θ.

Supplementary Note 4.

Permeability of devices: Due to the directional water transport in the devices with a gradient TiO_2 distribution, water gathers and evaporates more intensively for a higher evaporation rate (Supplementary Fig. 6). In the devices without a gradient TiO_2 distribution, water distributes uniformly in the fabric, leading to a lower evaporation rate.

The SSF maintains >88% air permeability and >94% moisture permeability after spraying TiO_2 nanoparticles and printing hygroelectric generators on the liquid diode (Supplementary Fig. 7). The good air permeability and moisture permeability are attributed to the small size of TiO_2 nanoparticles and high porosity of SSF devices.

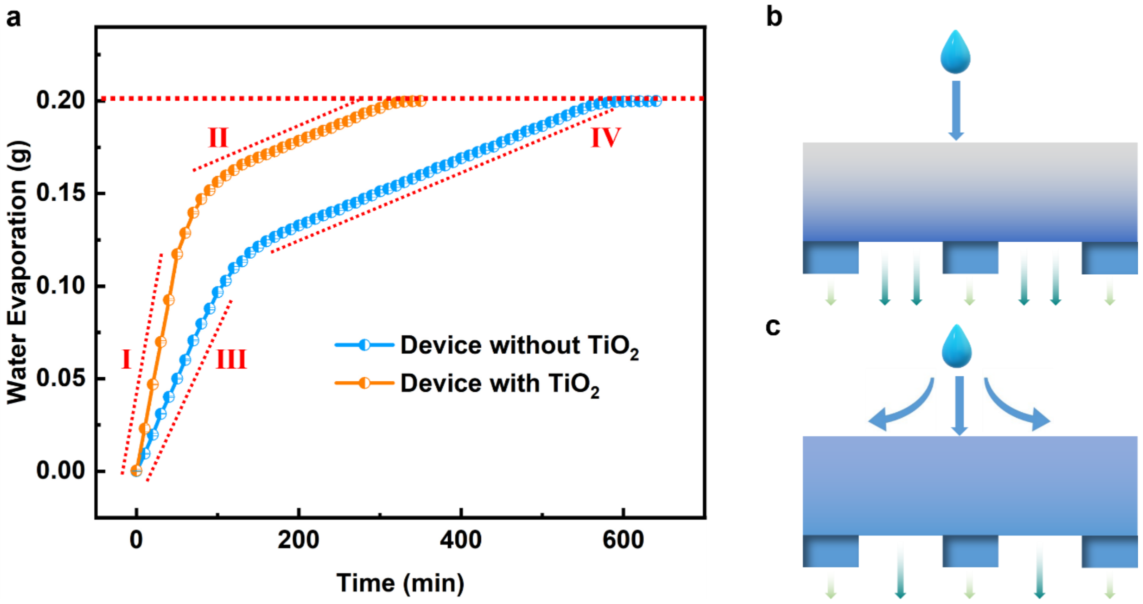

Supplementary Fig. 6 Water evaporation in the SSF with and without TiO_2. **a**, Water evaporation after dropping 0.2 g water on the bottom of devices. **b**,**c**, Schematical illustration of water evaporation in the devices with TiO_2 (**b**) and without TiO_2 (**c**).

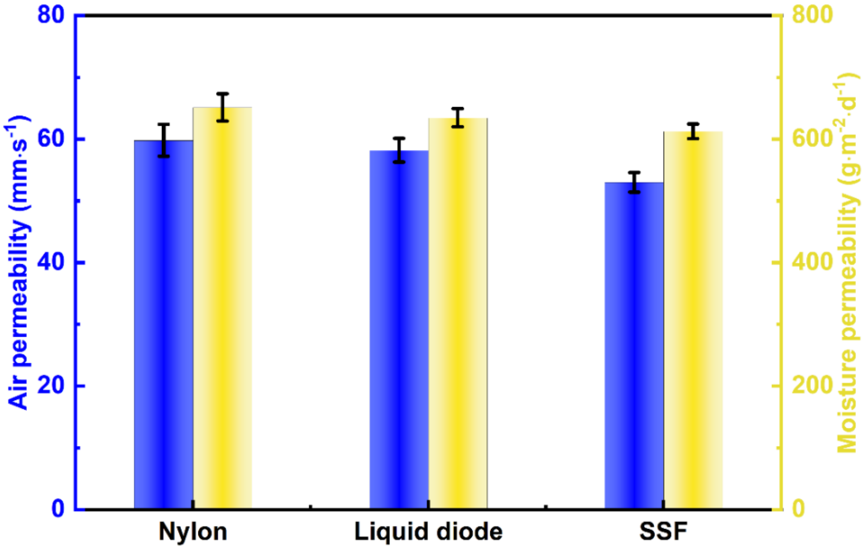

Supplementary Fig. 7 Comparison of air permeability and moisture permeability in the different fabrics. The experiments were carried out at 25 °C and 55% RH.

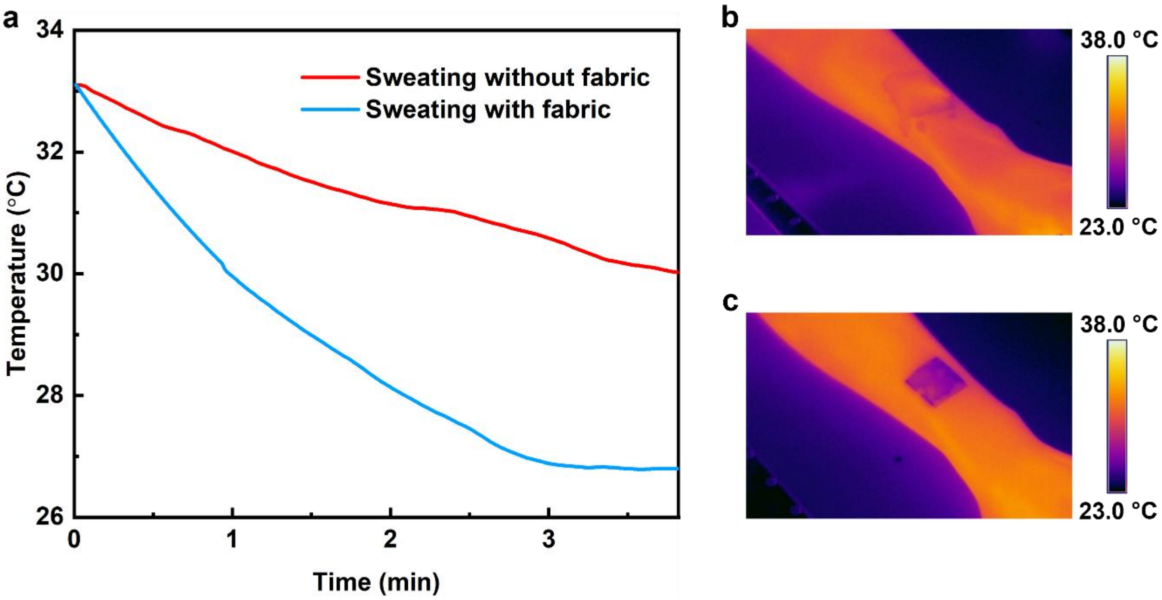

Supplementary Fig. 8 Temperatures after sweating with and without liquid diode. a, Temperature curve on the skin surface after sweating with and without liquid diode. **b**,**c,** IR images after sweating for 4 min for skin without liquid diode (**b**) and with liquid diode (**c**).

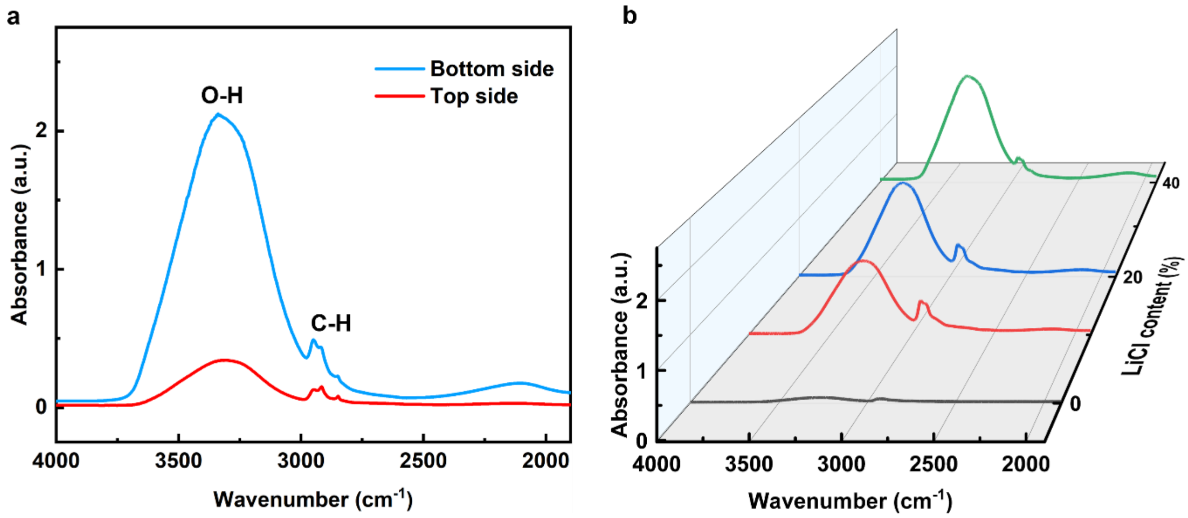

Supplementary Fig. 9 FTIR of hydrophilic layer. **a**, The FTIR of top and bottom side after dropping water on the bottom side of liquid diode for 10 min. **b**, The FTIR of top side of hydrophilic layer with different LiCl contents after dropping water on the bottom side of liquid diode for 10 min.

Supplementary Note 5.

Electricity generation by water gradient: The electricity generation by water transport is demonstrated by variation of water gradient and electric outputs. In the symmetrical relative humidity (Supplementary Fig. 10), no one-way water transport occurs in the functional layer. Thus, current output is ~0 mA·cm^{-2} in this condition. By placing SSF above water, the bottom and top side of SST is exposed to 99% RH and 55% RH, respectively. The asymmetrical humidity drives water migration from bottom electrode to the top electrode, which carries ion migration and charge separation for a high current output (0.15 mA·cm^{-2}).

Water was dropped in an opposite direction (from top electrode to bottom electrode), which led to a short negative current response (-0.16 mA·cm^{-2}) as water saturated the functional layer in a short time (Supplementary Fig. 11a). Electricity generation only occurs in the device with top/bottom electrodes, while devices with top/top or bottom/bottom electrodes delivers no electric output (Supplementary Fig. 11b), which also demonstrates that charge separation occurs in the direction of water evaporation.

By soaking top electrode in the water tank, a negative current peak of -0.11 mA·cm^{-2} was detected (Supplementary Fig. 11c). SSF shows no current output when top electrode and bottom electrode are soaked in the water horizontally (Supplementary Fig. 11d) as no water gradient exists between two electrodes. Thus, SSF delivers no obvious negative current output in different conditions and highlights the potential of SSF as a DC power.

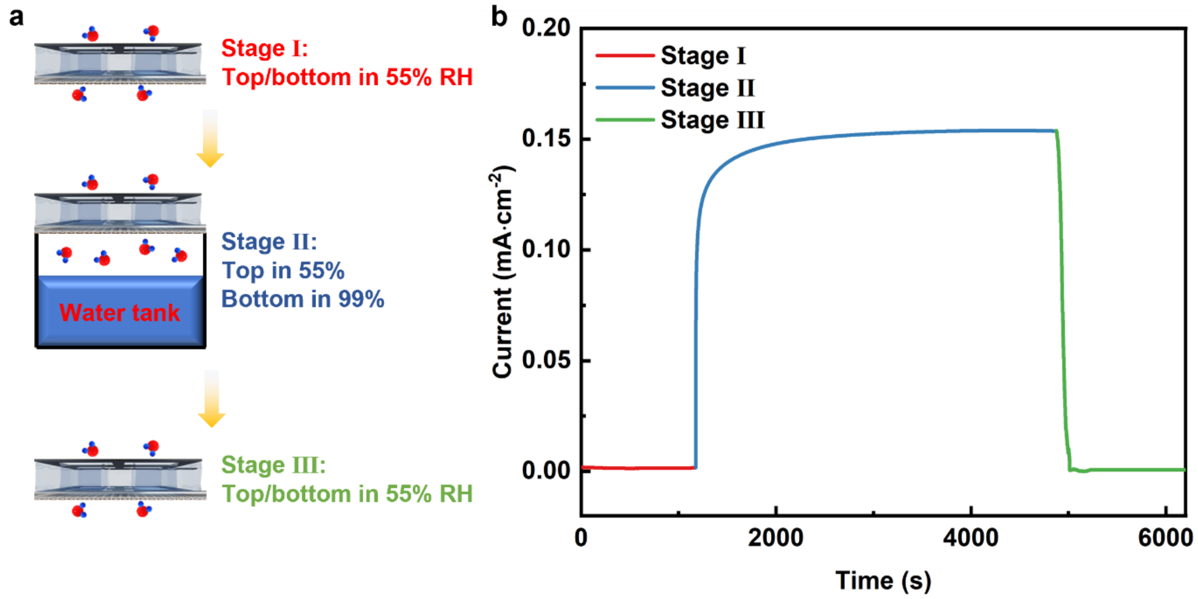

Supplementary Fig. 10 Current output of devices with moisture. a, Schematical illustration of devices exposed to different environmental moisture. **b**, Current output of devices exposed to different environmental moisture. In the stage I, the devices were exposed to symmetrical environmental moisture of 55% RH. In the stage II, the top sides of devices were exposed to environmental moisture of 55% RH. The bottom sides of devices were exposed to 99% RH by covering water tank with a distance of 1 cm. In the stage III, the devices moved back to the symmetrical environmental moisture of 55% RH.

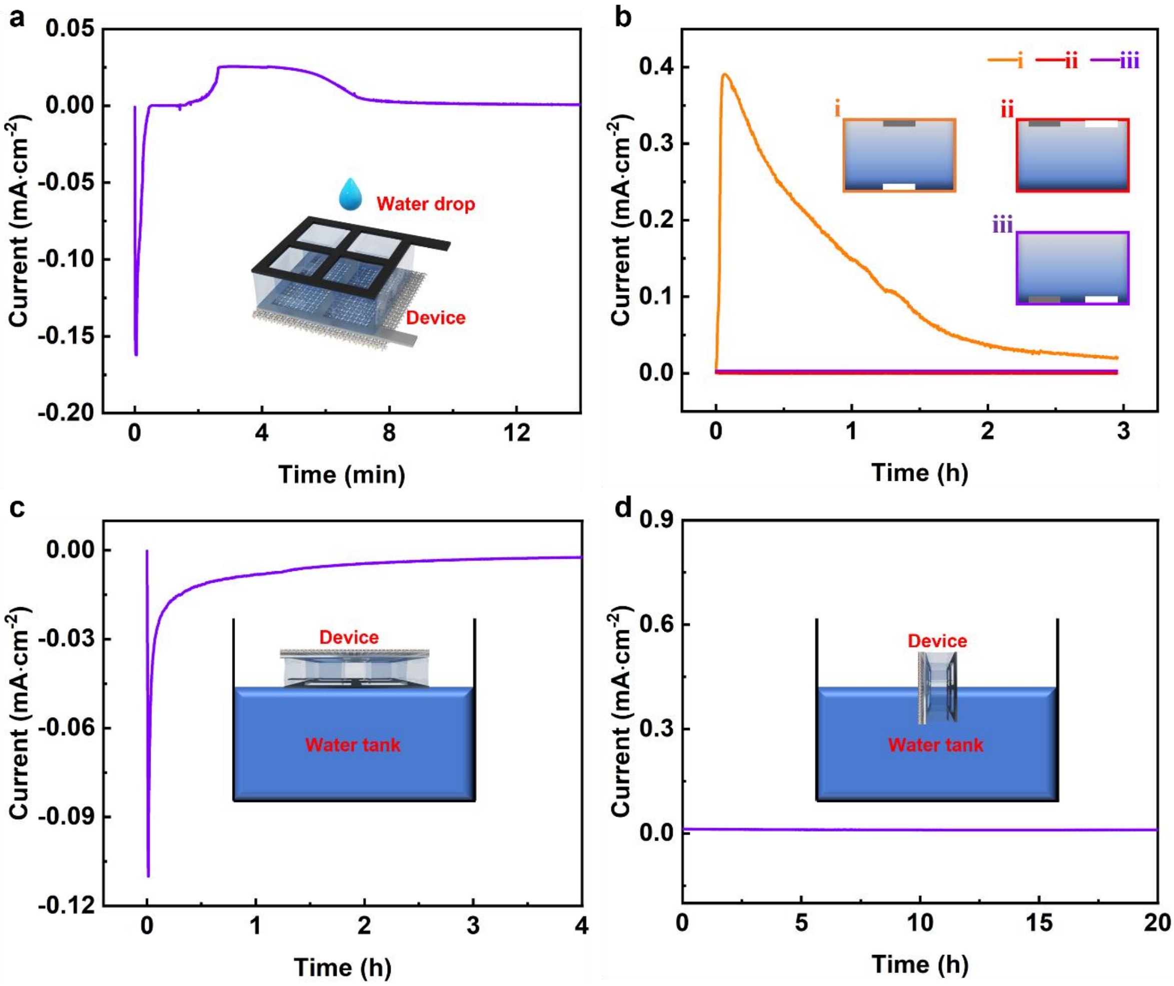

Supplementary Fig. 11 Current output of SSF devices with different sides exposed to D.I. water. **a**, Current output of device by dropping 0.2 g water on the top surface. **b**, Current outputs of device with different electrode configurations. **c**, Current output of device by placing top electrode above the water tank with 0.5 litre of water. **d**, Current output of device by immersing device in the water tank with 0.5 litre of water.

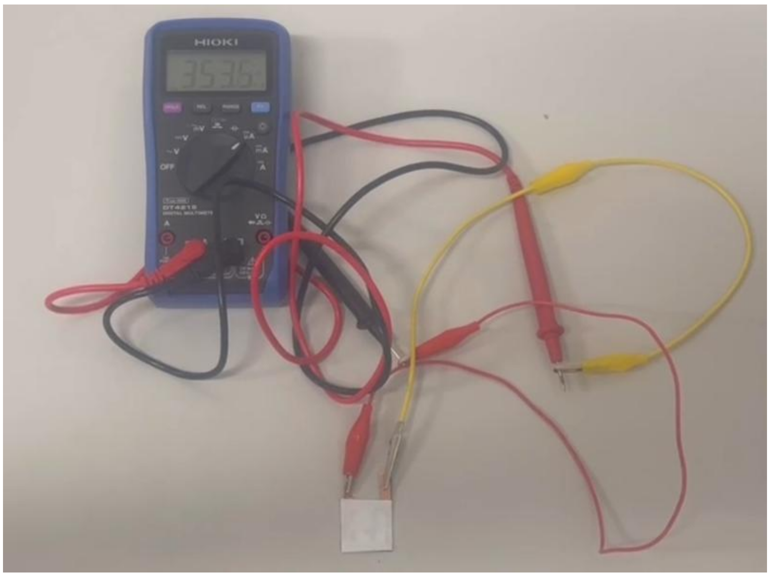

Supplementary Fig. 12 Photo of current output of SSF by a multimeter. The multimeter shows that a current of 353.5 μA is generated by SSF after dropping water onto the bottom side of SSF.

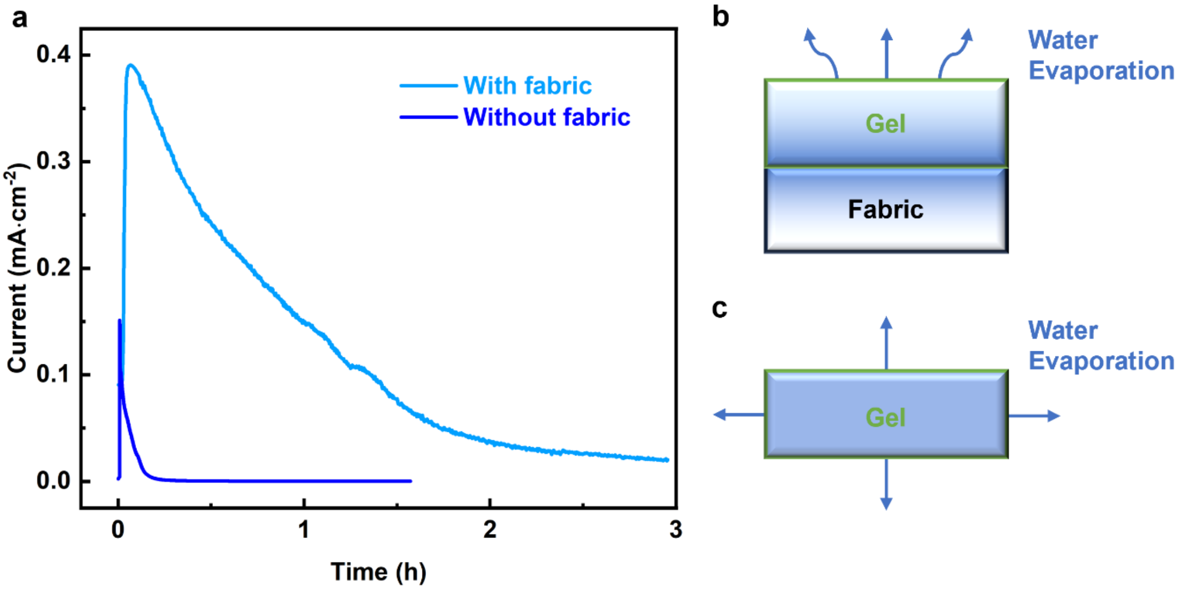

Supplementary Fig. 13 Devices with liquid diode and without liquid diode. a, Current outputs of devices after dropping water on the bottom of devices. **b**,**c**, Water distribution and evaporation through devices with liquid diode (**b**) and without liquid diode (**c**).

Supplementary Note 6.

Performances with different electrodes: The electrodes in the SSF are also important in regulating electricity generation. The SSF with Al as bottom electrode delivers higher electric outputs than that with Ni, Cu, Ag and graphene (Supplementary Fig. 14) as the printed Al electrode shows a lower electric resistance of 23 Ω·cm^{-1} (Supplementary Fig. 15a). Besides, the SSF with graphene as top electrode delivers higher electric outputs than that with CNT, Ag and Al (Supplementary Fig. 15b) as graphene contributes to a higher evaporation rate of 0.11 kg·m^{-2}·h^{-1} (Supplementary Fig. 15c), which facilitates ion migration and enhances electric outputs. The faster water evaporation in the graphene electrodes is attributed to the absorption broadband light[12]. The SSF with graphene as top electrode also delivers a higher current output with illumination, compared with device working without illumination.

The cyclic voltammetry curve of device shows no reaction peak (Supplementary Fig. 16a), while no Al element distributes in the functional layer after operation (Supplementary Fig. 16b), which demonstrate that electricity generation relies on ion migration instead of chemical reactions between electrode and functional layer.

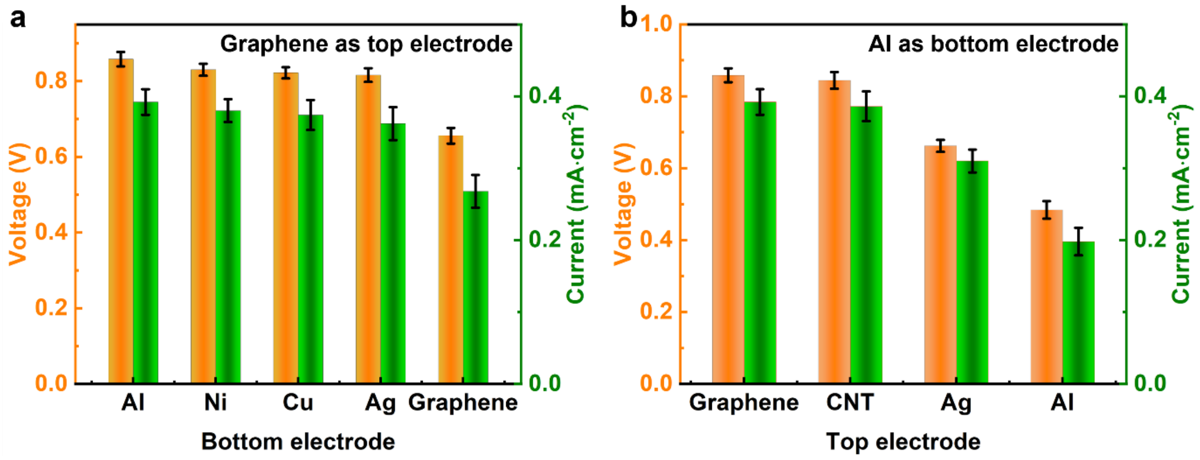

Supplementary Fig. 14 Electric outputs of devices with different electrode materials. a, Outputs of devices with graphene as top electrode and different materials as bottom electrode. **b**, Outputs of devices with Al as bottom electrode and different materials as top electrode.

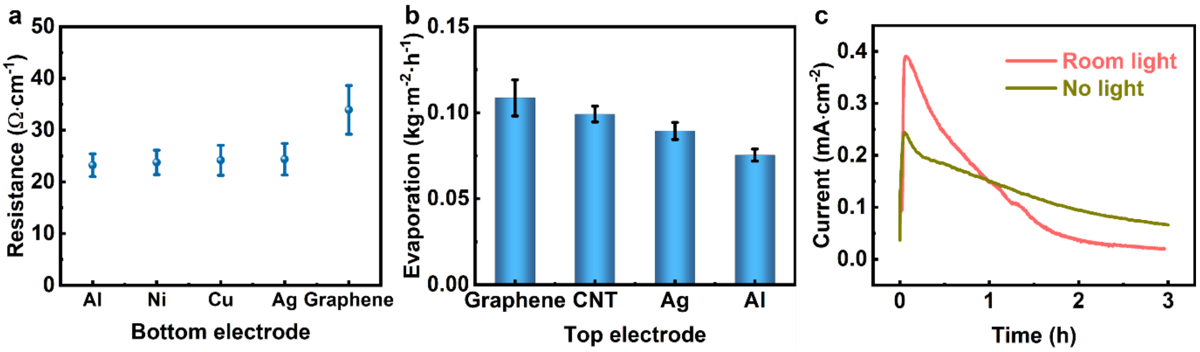

Supplementary Fig. 15 Performance of different electrode materials. a, Electric resistance of different printed materials on the nylon fabrics. **b**, Water evaporation of devices with Al as bottom electrode and different materials as top electrode. **c**, Current output of devices under room light and no light. Al foil was placed above the devices with 10 cm distance in the test without light.

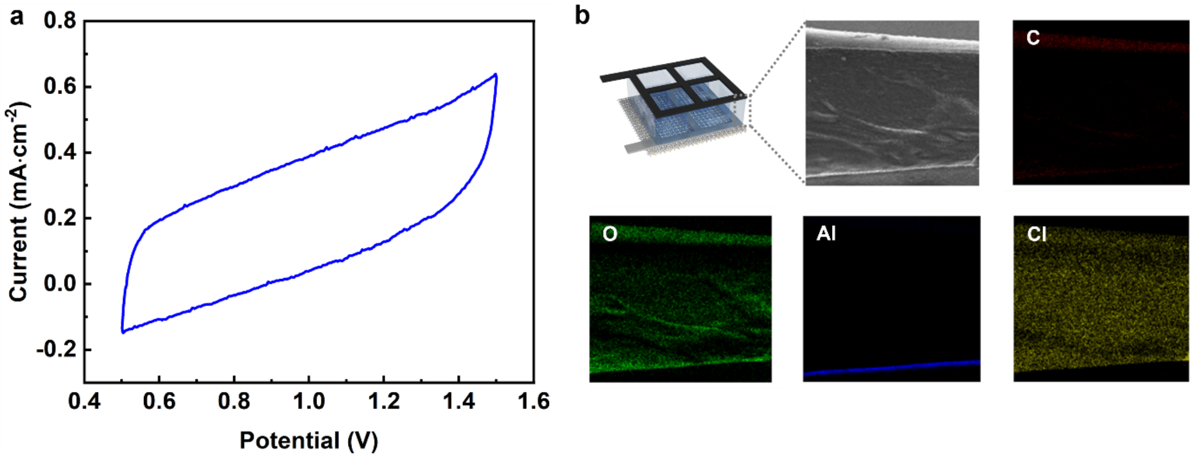

Supplementary Fig. 16 Capacitive behavior of SSF. a, Cyclic voltammetry curve of devices with 0.2 g water drop. The curve was recorded 20 min after water was dropped onto the fabric. **b**, Structure and element distribution of devices with Al, PVA/LiCl and graphene as bottom electrode, functional layer and top electrode, respectively.

Supplementary Note 7.

Water states in the functional layers: The water states in the functional layer are divided into free water (FW) and intermediate water (IW) in the Raman spectra (Supplementary Fig. 17). FW is isolated from polymer chains, while IW has a weak interaction with adjacent water molecules or polymer chains and can be vaporized with less energy[13]. The increased amount of LiCl endows a higher ratio of IW (Supplementary Fig. 17b) due to the hydration of LiCl, which facilitates water evaporation for the enhanced electric outputs.

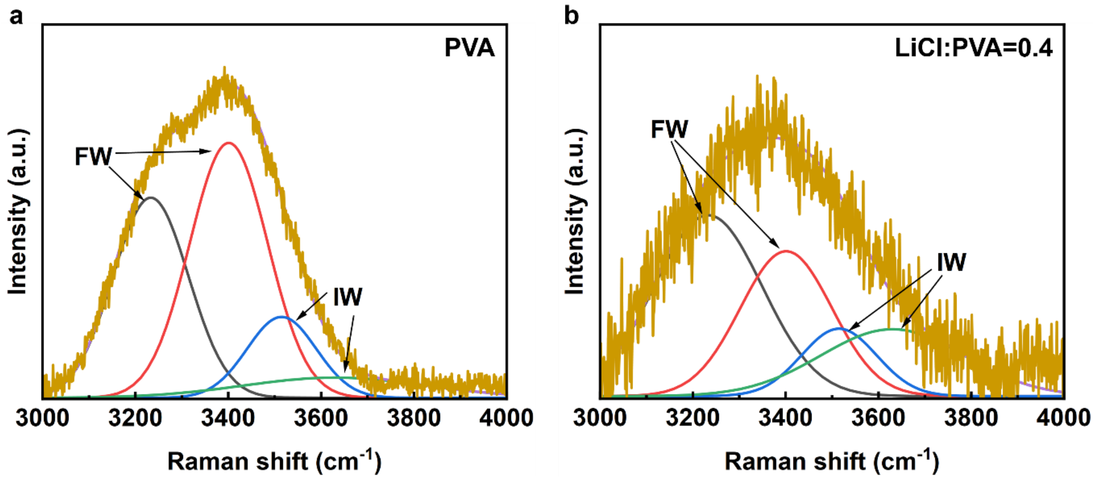

Supplementary Fig. 17 The comparison of IW and FW in the different functional layers. a,**b**, Raman spectra with fitting peaks of PVA (**a**) and LiCl:PVA=0.4 (**b**).

Supplementary Note 8.

Molecular dynamics (MD) simulations: The ionic and small molecule structures were modeled by GaussView 6.0 software, followed by optimization by Gaussian16 software employing the B3LYP/6-311g(d,p) method and frequency calculations at the same level to obtain wavefunction files. The polymer chains were constructed by Material Studio 2023 software, followed by structure optimization and frequency calculations under similar conditions. The force field parameters of ions and small molecules were built from the GAFF2 force field and Sobtop software[14]. RESP charges for ions and molecules were calculated using the Multiwfn software based on the wavefunction files[15], followed by replacing the original charges for subsequent molecular dynamics simulations. All charges were scaled by a factor of 0.8 to achieve polarization and charge transfer[16].

The initial configurations with atomic tolerance of 2.0 Å and vacuum layer of 1.5 Å were constructed to avoid unreasonable mirror interactions in the Packing Optimization for Molecular Dynamics Simulations (Packmol) program[17]. The dimensions of the periodic box were set to 85 × 85 × 60 $Å^3$, divided into two layers along the z-axis with 70 polymer chains, 100 Li^+ ions, and 100 Cl^- ions were placed in each layer. To mimic water gradient, 1200 water molecules were in the upper layer, 6000 water molecules were in the lower layer.

All simulations were performed by GROMACS 2022.4 software[18], followed by the procedure outlined in the references[19, 20]. The system was optimized through 5000 steps of steepest descent followed by 5000 steps of conjugate gradient minimization to avoid unreasonable contacts for energy minimization. The pre-equilibration was performed by NPT ensemble with V-rescale temperature coupling and Parrinello-Rahman pressure coupling to achieve a temperature of 298 K and a pressure of 1 atm, respectively. The non-bonded interaction cutoff radius was 1.2 nm, with a 1 fs integration timestep. Then, the bond lengths and angles in the system were constrained using the LINCS algorithm. The dual cutoff size is 1.2 nm. The long-range electrostatic interactions were calculated by particle-mesh Ewald method.

Density functional theory (DFT) calculations: Electrostatic potential of PVA and PVA/LiCl is carried out in Multiwfn and VMD packages to analysis the charge distribution[21, 22]. The Gaussian 16 software was adopted to perform DFT computations. The molecule structures with gas phases were analyzed by B3LYP functional and D3BJ dispersion correction[23, 24]. 6-31G(d,p) basis set was adopted to achieve optimization of polymer structure. The level of M062x-D3/6-311G(d,p) was set in the single point calculations[25].

To analyze the migration barrier of ions along PVA chains, the spin-polarized DFT calculations were performed by Vienna ab initio simulation package (VASP) based on the plane-wave basis sets and projector augmented-wave theory[26, 27]. The generalized gradient approximation (GGA) with the Perdew-Burke-Ernzerhof (PBE) parametrization is used for exchange-correlation potential[28]. Grimme's DFT-D3 model was used to achieve van der Waals correction in the DFT calculations. Lattice parameter of computed structures is (a, b, c) = (20.0 Å, 15.0 Å, 15.0 Å), with 450 eV energy cutoff. The 1 × 1 × 1 Gamma k-point grids was adopted to sample the Brillouin zone integration[29]. The structures and transition state calculation were fully relaxed until the maximum force on each atom was less than 0.02 eV/Å, and the energy convergent standard was 10^{-5} eV. The transition states was calculated by a modification of climbing image nudged elastic band method[30].

From the electrostatic potential distribution of PVA and PVA/LiCl (Supplementary Fig. 18), the electrostatic gradient of PVA/LiCl is higher and facilitates charge separation for electricity generation, the wider distribution of electrostatic potential in the functional layer of PVA/LiCl indicates the greater water absorption ability for enhanced ion migration rates.

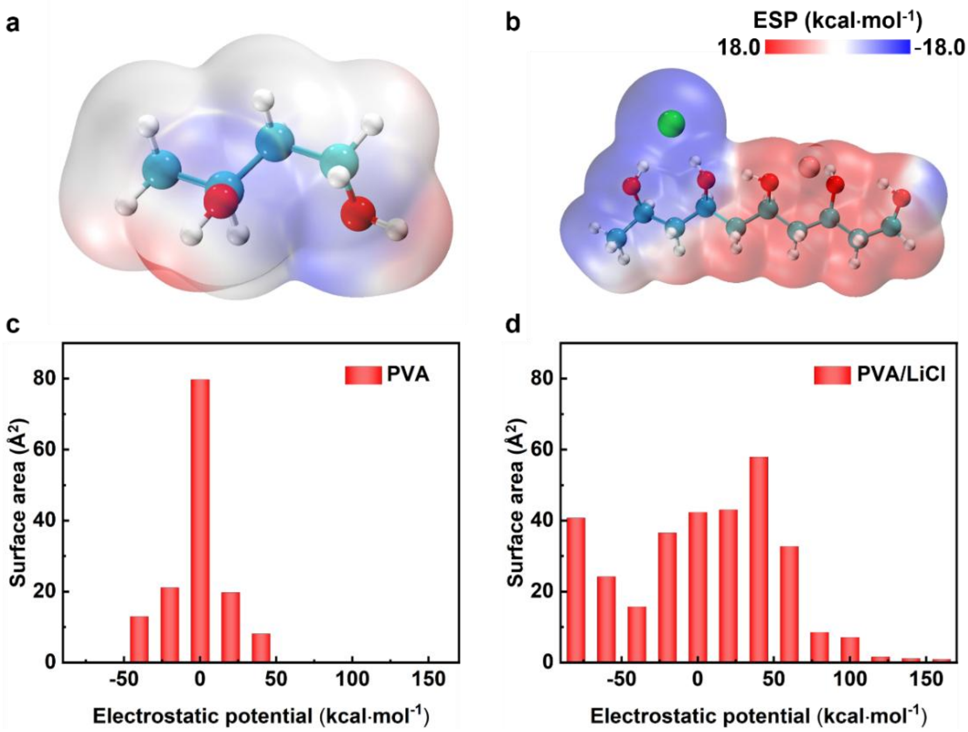

Supplementary Fig. 18 The electrostatic potential calculation of PVA and PVA/LiCl. a,**b**, The electrostatic potential distribution of PVA (**a**) and PVA/LiCl (**b**). **c**,**d**, Surface area and corresponding area percent in each ESP range on the vdW surface of PVA (**c**) and PVA/LiCl (**d**).

Supplementary Note 9.

Performances with different water sources: The ion migration for electricity generation is closely related to the interaction between charge carriers (Li^+/Cl^- ions) and transport medium (water). The increased water contents or salts ratios leads to the decreased ionic resistance (Supplementary Fig. 19) for enhanced current outputs as more ions are bonded with water molecules to achieve greater ion migration and electricity generation.

By adding LiCl into the water (transport medium) dropped on the SSF, the device delivers a higher current output as more Li^+ and Cl^- ions are absorbed by the functional layer (Supplementary Fig. 20a). Moreover, the current of SSF increases and then decreases with the increase of ethanol ratio in the applied solution (Supplementary Fig. 20b). The added ethanol facilitates evaporation of solution (Supplementary Fig. 20c) to achieve faster ion migration and higher current outputs. Besides, ethanol molecules exhibit a weaker interaction with ions, compared water molecules. Thus, excess ethanol in the mixed solution could not transport ions efficiently and reduces current outputs.

As for the cooling performance, the higher ratio of ethanol added in the applied solution leads to the faster evaporation and higher temperature reduce (Supplementary Fig. 20d).

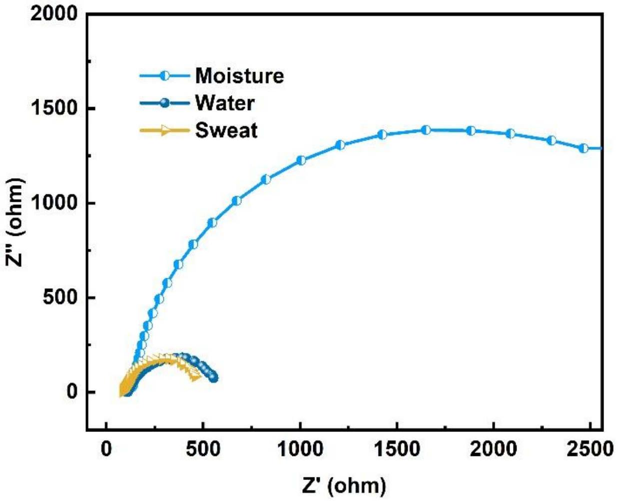

Supplementary Fig. 19 EIS of SSF devices. The SSF devices were exposed to the different water sources for 10 min before EIS test. The RH was 90% for the EIS test in the moisture. The 0.2 g D.I water or sweat was dropped on the bottom of SSF.

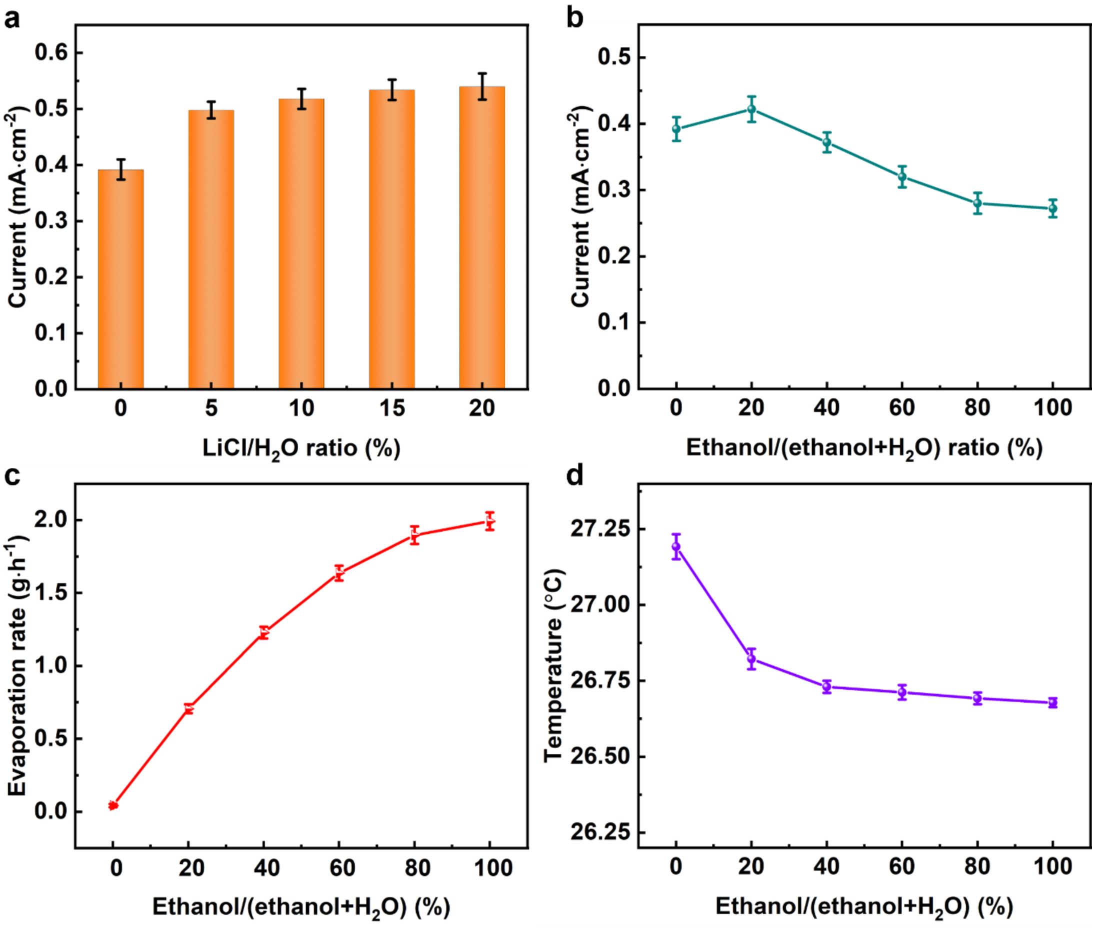

Supplementary Fig. 20 Performance of devices with different water source. a, Current output of devices by dropping 0.2 g solution with different LiCl/H_2O ratios. **b**, Current output of devices by dropping 0.2 g solution with different ethanol/(ethanol+H_2O) ratios. **c**, Water evaporation of devices by dropping 0.2 g solution with different ethanol/(ethanol+H_2O) ratios. **d**, Temperature of skin surface by dropping 0.2 g solution with different ethanol/(ethanol+H_2O) ratios on the interface of device and skin.

Supplementary Note 10.

Mechanism illustration by simulation: To further illustrate the mechanism of electricity generation, MD simulations and DFT calculations are performed to investigate synergistic effect of ion migration and water transport. Two boxes with different ratios of water molecules are stacked (t=0 ns) to simulate the process of electricity generation (Supplementary Fig. 21). The water transports from the bottom box with a higher ratio of water molecules to the top box with a lower ratio of water molecules. Meanwhile, Li^+ and Cl^- ion migration along the direction of water transport were observed.

The charge separation between Li^+ and Cl^- ions can be illustrated by the difference of energy barrier along the PVA chains. In the ion migration path between two adjacent sites along the PVA chain (Supplementary Fig. 22a), the calculated energy barrier of Li^+ and Cl^- ions is about 0.4 eV and 0.2 eV, respectively (Supplementary Fig. 22b), which demonstrates that Cl^- ion migration is activated with less energy. Thus, top box contains more Cl^- ions with less Li^+ ions, which achieves charge separation.

The binding energy between ions and different molecules is investigated to illustrate ion migration. The binding energy of Li^+-H_2O, Cl^--H_2O, Li^+-PVA, Cl^--PVA is -63.83 eV, -25.49 eV, -24.42 eV, -3.81 eV, respectively (Supplementary Fig. 23). H_2O molecules with ions exhibit a higher binding energy than PVA molecules with ions, which demonstrates that H_2O molecules work as the key transport medium for the ion migration.

Radial distribution function (RDF) and coordination number (CN) of Li^+ ions with H_2O and gel are calculated (Supplementary Fig. 24). The CN of Li^+ ions with gel is lower than that of Li^+ ions H_2O, which demonstrates that polymer chains in the gel occupy inner solvent sheath of hydrated Li^+ ions and work as transportation paths of ion migration.

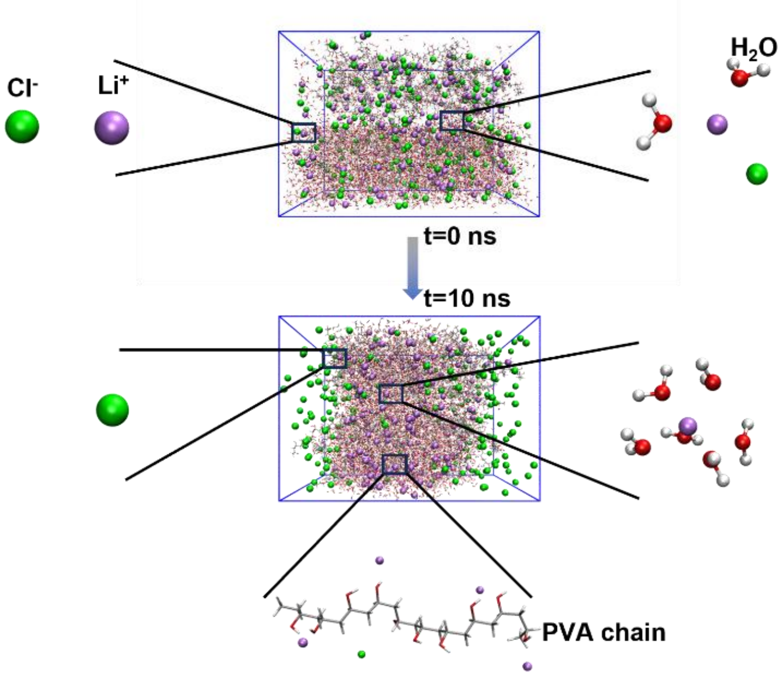

Supplementary Fig. 21 3D snapshots and screenshots with distribution of Li^+/Cl^- ions, H_2O molecules and PVA chains from MD simulations at 0 ns and 10 ns. The experiment starts with two layers with different water contents to construct a water gradient.

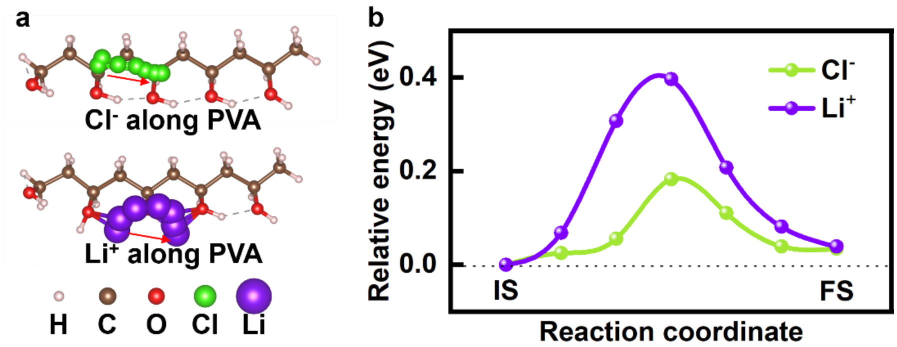

Supplementary Fig. 22 Ion migration along PVA chains for charge separation. a, Illustration of Li^+ and Cl^- migration along PVA chains. **b**, Energy barrier of Li^+ and Cl^- migration along PVA chains, calculated from density functional theory.

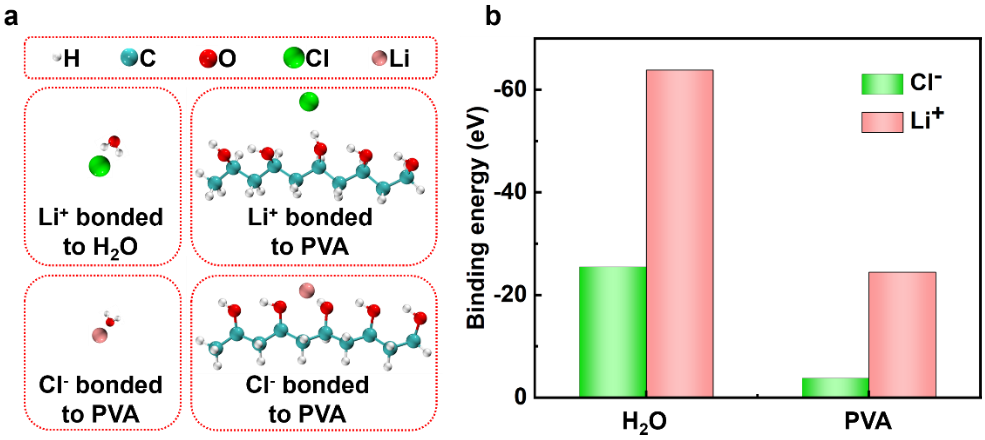

Supplementary Fig. 23 Binding energy of ions and H_2O/PVA. a, Illustration of Li^+ ions and Cl^- ions bonded to H_2O and PVA chains. **b**, Binding energy of Li^+/Cl^- ions and H_2O/PVA chains, calculated from density functional theory.

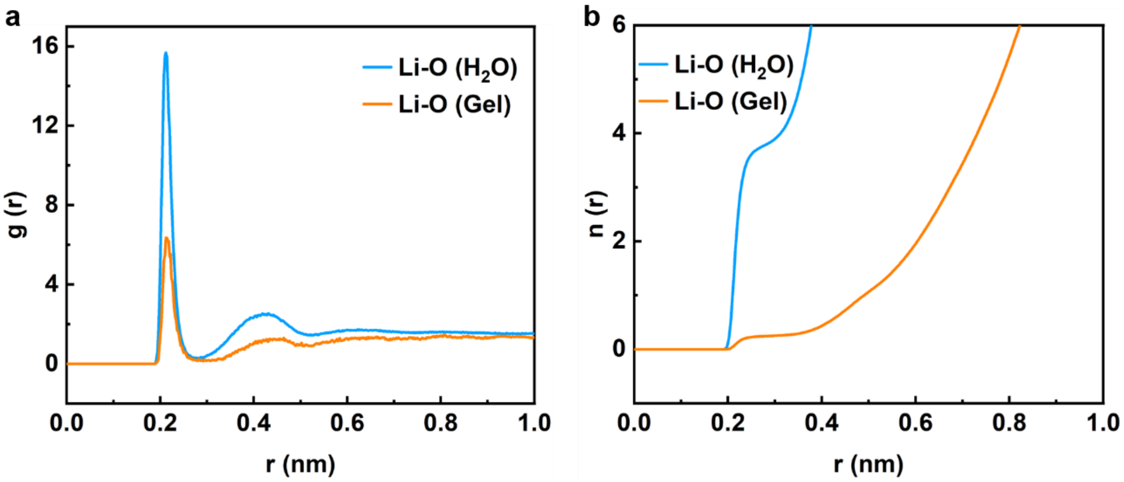

Supplementary Fig. 24 Coordination environment surrounding of Li ions in H_2O and gel from MD simulation. a, Radial distribution function. **b**, Coordination number.

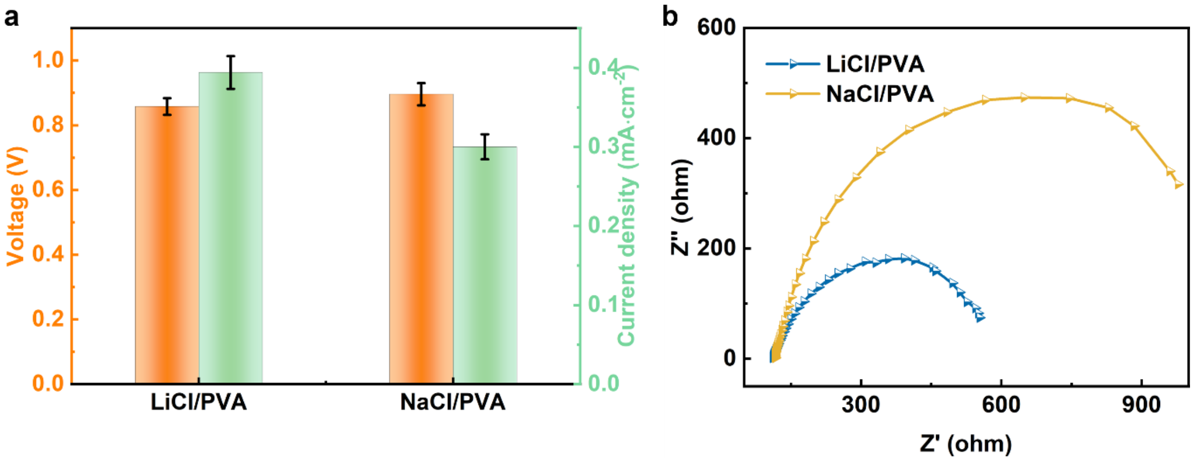

Supplementary Fig. 25 Electric outputs of SSF fabricated with different gels. a, Open-circuit voltage and short-circuit current of SSF with different salts. **b**, EIS of SSF with different salts.

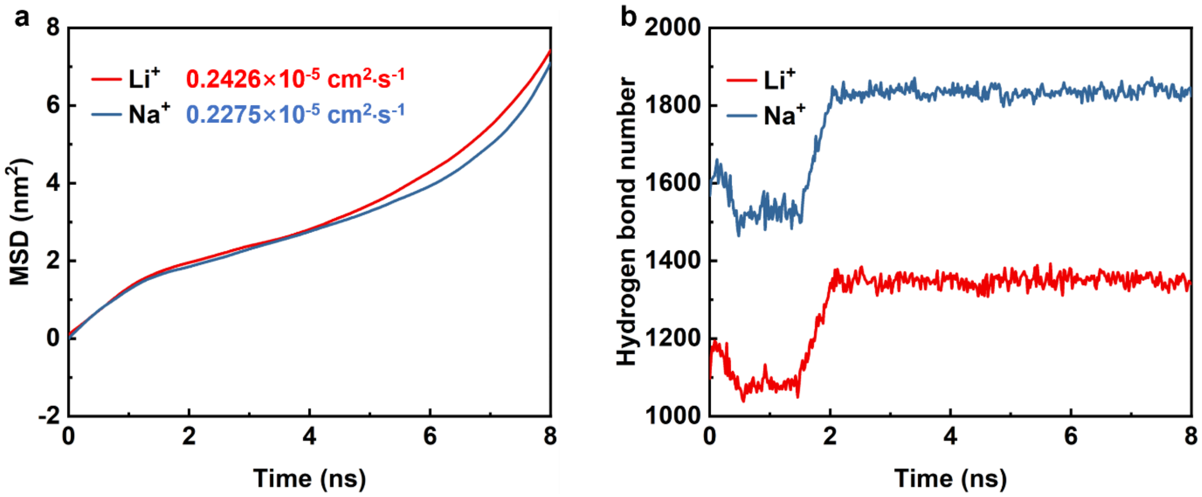

Supplementary Fig. 26 Ion migration in different systems with Li^+ and Na^+ from MD simulation. **a**, The function of MSDs vs. time in LiCl/PVA and NaCl/PVA. **b**, Hydrogen bond number in LiCl/PVA and NaCl/PVA.

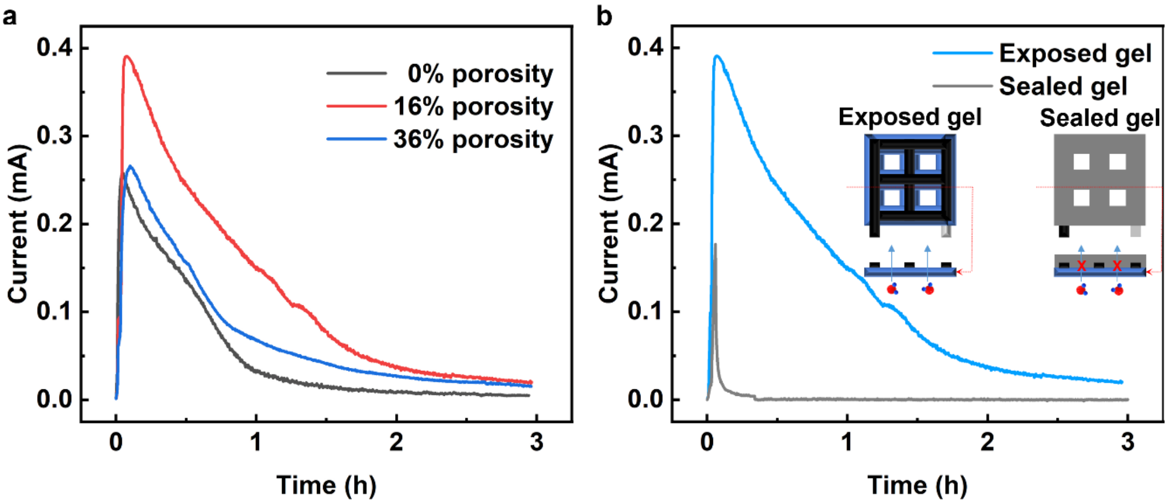

Supplementary Fig. 27 Current outputs of SSF. a, Current outputs of devices with different porosity. **b**, Current outputs of devices with and without sealing on the top surfaces by carbon tape.

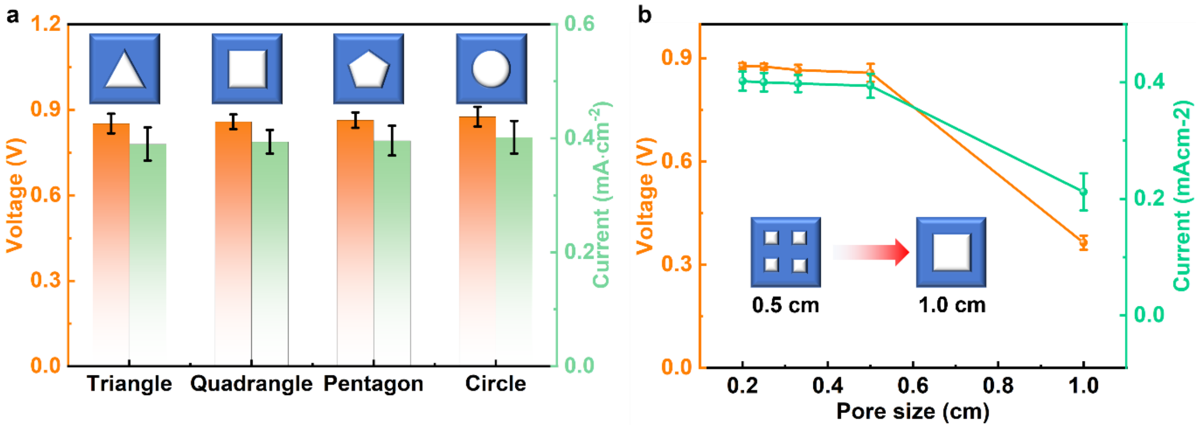

Supplementary Fig. 28 Electric outputs of devices with different pores. **a**, Outputs of devices with different shapes of exposed areas. **b**, Outputs of devices with different pore size. The total areas of exposed pore areas are the same.

Supplementary Note 11.

Thermal calculation of heat flux: The thermal resistance (Supplementary Fig. 29) of heat transfer along the thickness direction of SSF is calculated according to the thermal resistance network and following equation:

$$R_{device} = \left(\frac{\emptyset_{Al}}{\frac{\delta_f}{\lambda_f}+\frac{\delta_{Al}}{\lambda_{Al}}+\frac{\delta_{gel}}{\lambda_{gel}}+\frac{\delta_{gra}}{\lambda_{gra}}} + \frac{\emptyset_{gel}-\emptyset_{Al}}{\frac{\delta_f}{\lambda_f}+\frac{\delta_{gel}}{\lambda_{gel}}} + \frac{1-\emptyset_{gel}}{\frac{\delta_f}{\lambda_f}} \right)^{-1} \quad (1)$$

R_{device} is the thermal resistance of SSF. $\emptyset_{Al}$ and $\emptyset_{gel}$ are the area percentage of printed Al electrode and gel on the liquid diode. δ_f (0.5 mm), δ_{Al} (0.01 mm), δ_{gel} (0.15 mm), δ_{gra} (0.01 mm) are thickness of nylon fabric, Al electrode, gel, graphene electrode, respectively. λ_f (0.25 $W{\cdot}m^{-1}{\cdot}K^{-1}$), λ_{Al} (237 $W{\cdot}m^{-1}{\cdot}K^{-1}$), λ_{gel} (0.55 $W{\cdot}m^{-1}{\cdot}K^{-1}$), λ_{gra} (45 $W{\cdot}m^{-1}{\cdot}K^{-1}$) are thermal conductivity along the thickness direction of nylon fabric, Al electrode, gel, graphene electrode, respectively. Area ratios of Al electrode, gel and fabric are 12.75%, 75%, 25%, respectively.

Since SSF shows a heterogeneous structure, three paths of heat transfer are involved in the calculation of thermal resistance. First path is calculated with four layers of nylon fabric, Al electrode, gel, graphene electrode. Second path is calculated with two layers of nylon fabric, graphene electrode. Third path is calculated with a single layer of nylon fabric.

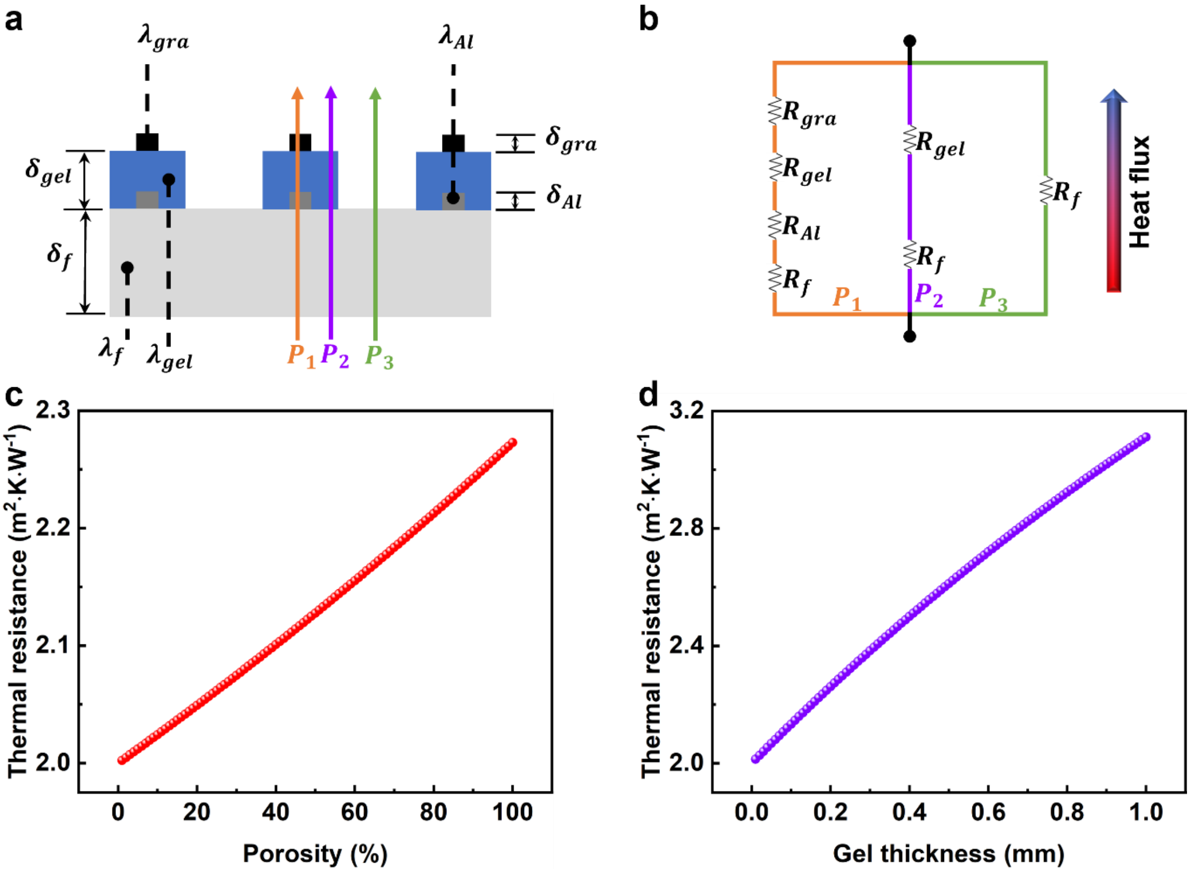

Supplementary Fig. 29 Thermal resistance calculation of SSF network. a, Schematical illustration of three heat flux paths through the cross-section. **b**, Equivalent thermal resistance network diagram of SSF. **c**, Thermal resistance of SSF with different porosity. **d**, Thermal resistance of SSF with different gel thickness.

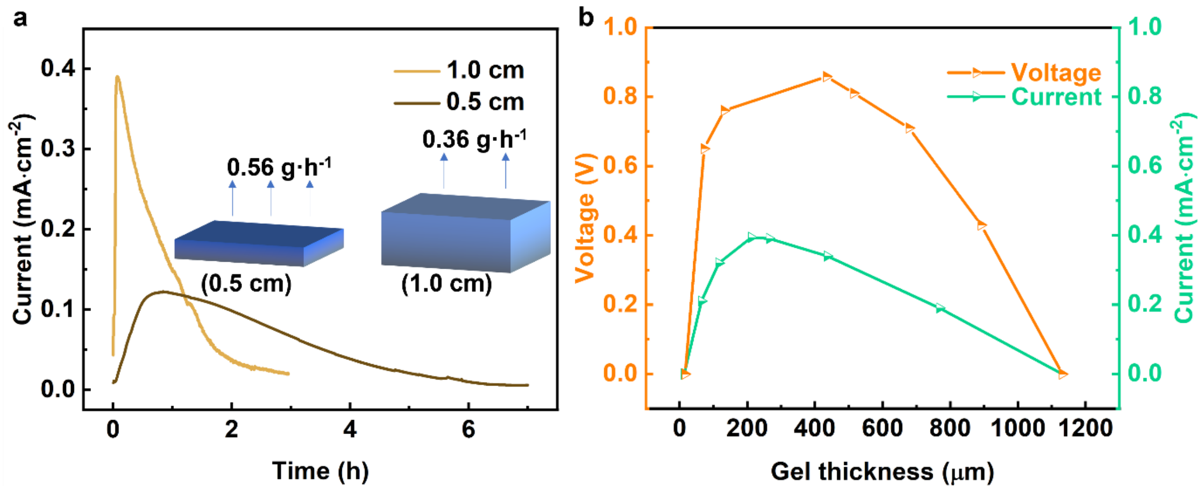

Supplementary Fig. 30 Electric outputs of devices with different thickness. **a**, Current outputs of devices with different fabric thickness. The fabric with 0.5 cm and 1.0 cm thickness delivered water evaporation rate of 0.56 g·h^{-1} and 0.36 g·h^{-1}, respectively. **b**, Electric outputs of devices with different gel thickness.

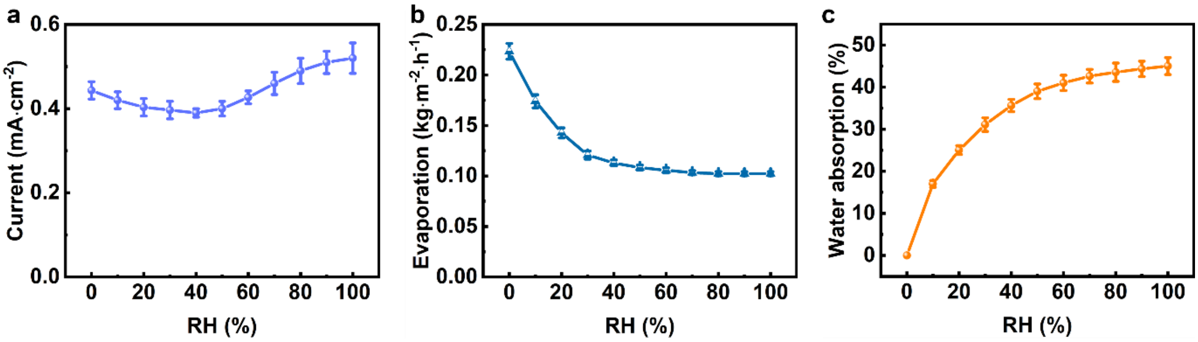

Supplementary Fig. 31 Performance of devices by dropping water at different relative humidity. a, Current output of devices by dropping 0.2 g water on the bottom surfaces and exposing devices to the environment with different RH. **b**, Water evaporation of free-standing gels after dropping 0.2 g water on the surfaces of gels. The water evaporation weigh was recorded after placing gels at different RH for 48 h. **c**, Water absorption of free-standing gels after placing gels at 0% RH for 48 h. The water absorption was recorded after placing gels at different RH for 48 h.

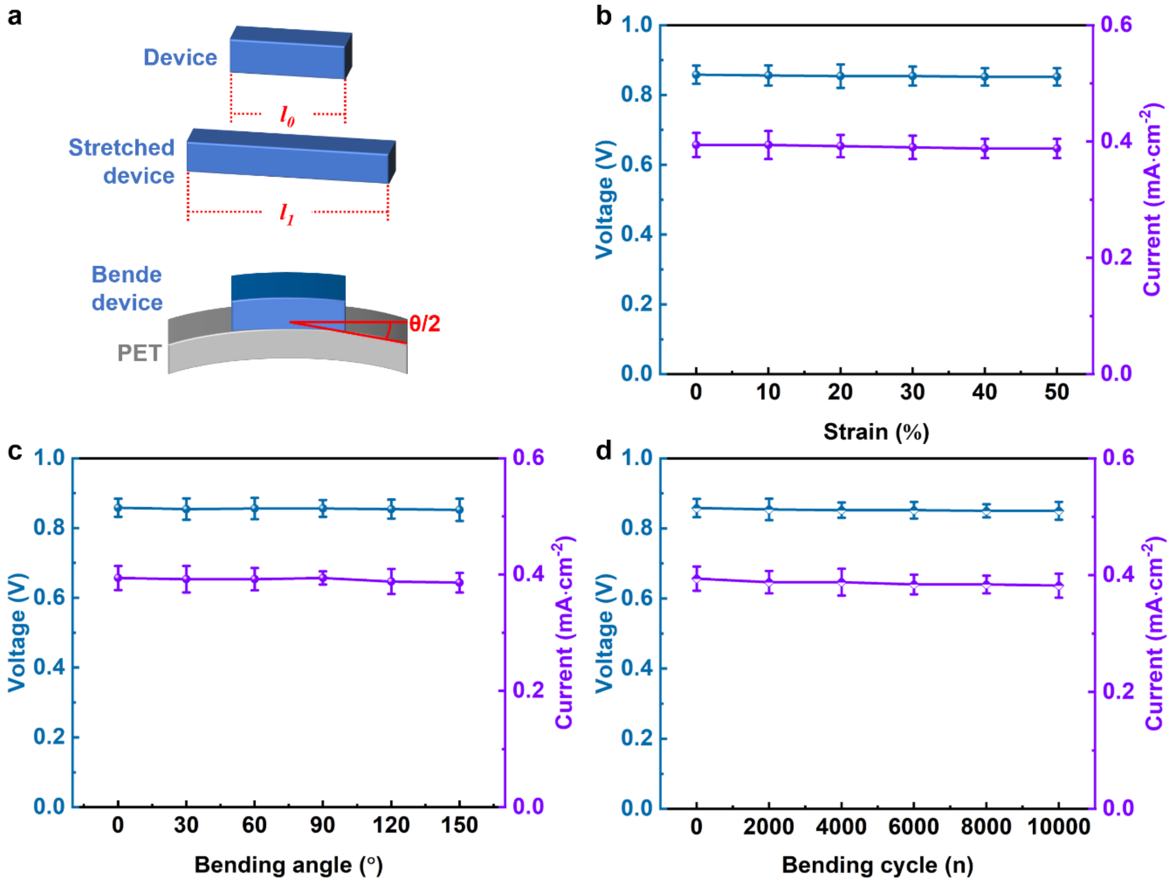

Supplementary Fig. 32 Electric output of devices with deformation. **a**, Schematical illustration of device with stretching and bending. The strain was determined by $(l_1-l_0)/l_0\times100\%$, where l_0 and l_1 represent length of device before and after stretching, respectively. The device was attached to the PET in the bending test. **b**, Electric output of devices after devices are stretched with different strain. **c**, Electric output of devices after devices are bent with different bending angles. **d**, Electric output of devices after different bending cycles with a bending angle of 90°.

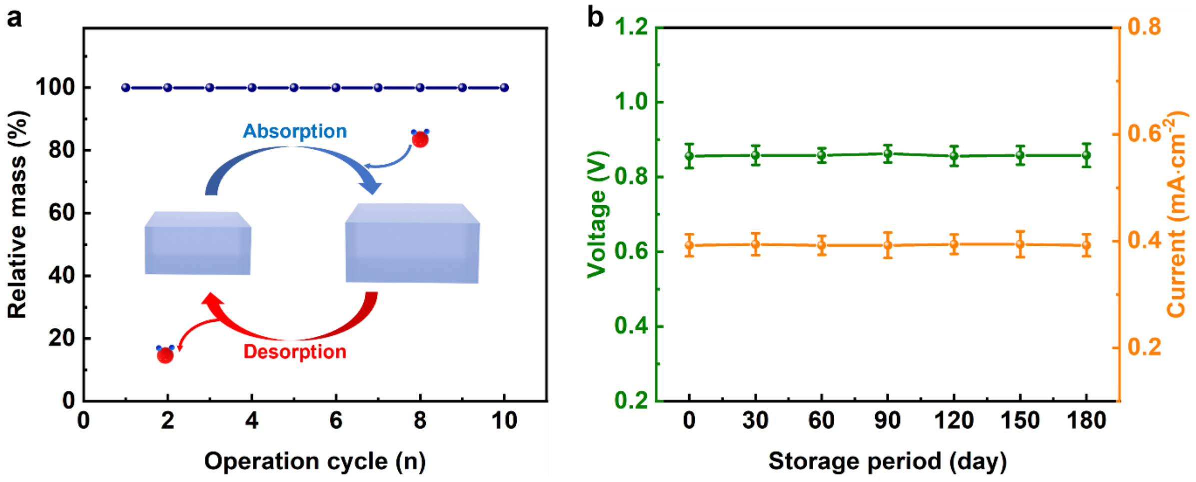

Supplementary Fig. 33 Operation stability of devices. **a**, The mass in the different operation cycles of water absorption and desorption. The mass of devices was recorded after each operation cycle. **b**, Outputs of devices with different storage periods. The devices were stored at 45% RH and 25 °C.

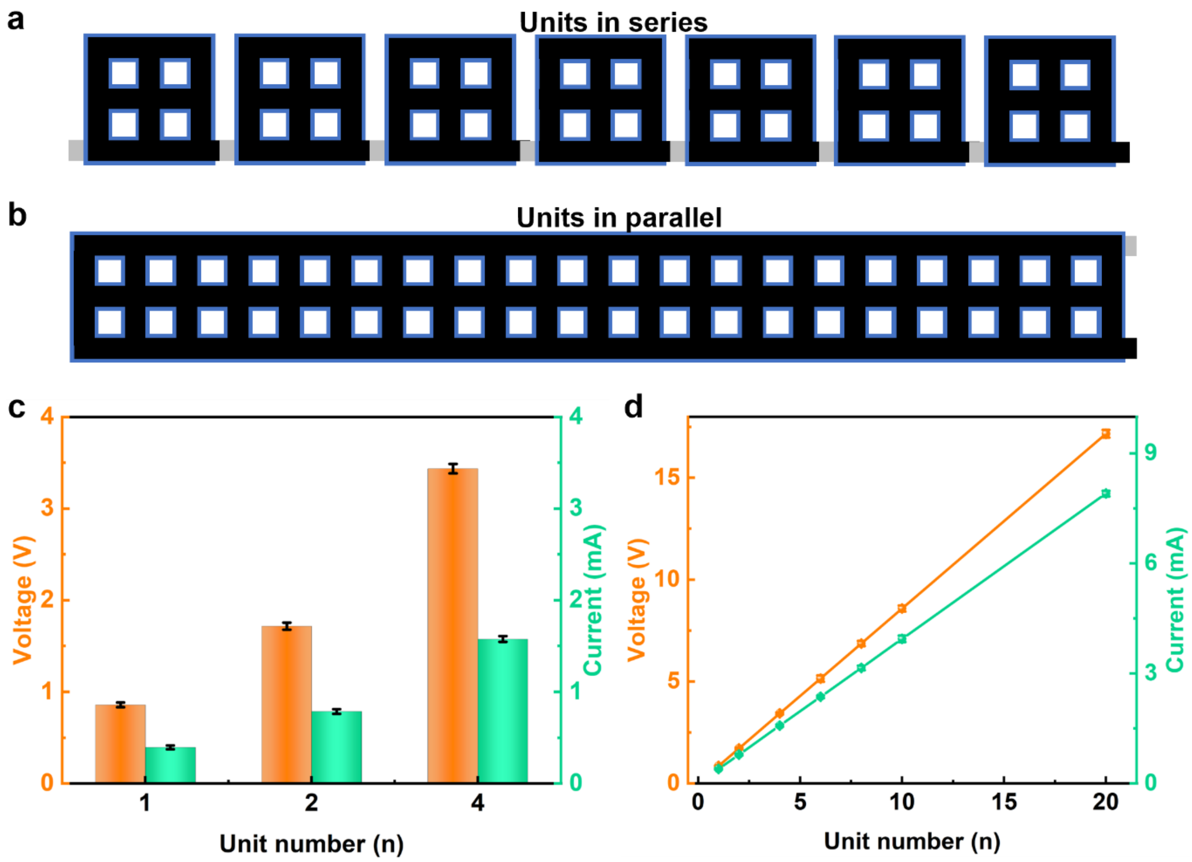

Supplementary Fig. 34 Electric output of device units connected in series or parallel. a,**b**, Schematical illustration of device units printed in series (**a**) or parallel (**b**). **c**, Voltage and current of units connected in series and parallel, respectively. **d**, Electric outputs of multiple units. Each SSF unit was dropped with 0.2 g water to charge the power storage devices.

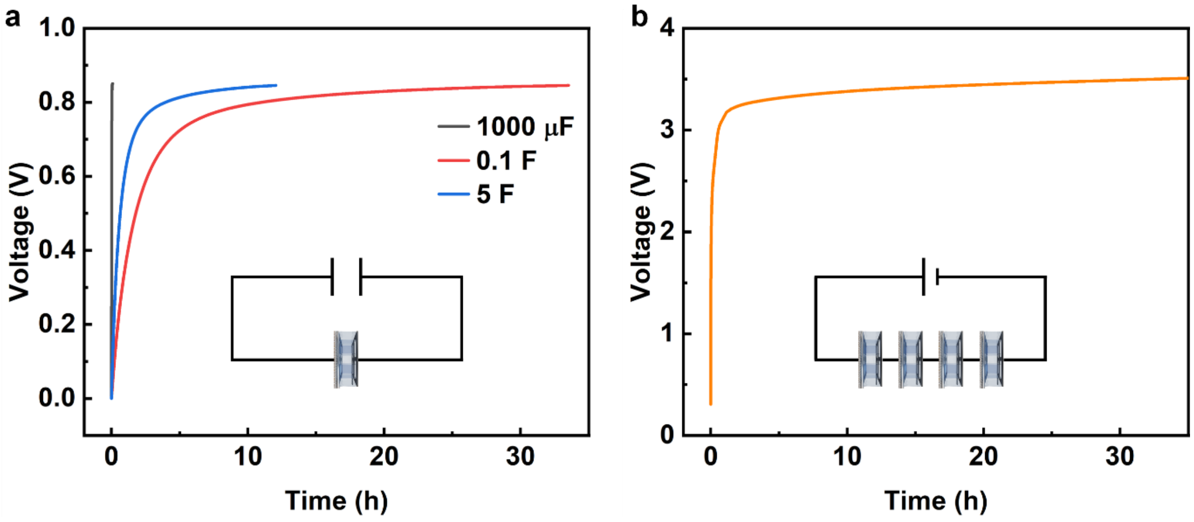

Supplementary Fig. 35 The charging curve of commercial power storage devices. a, Voltage curve of capacitors with different capacitance. The capacitor was charged by a single SSF unit. **b**, Voltage curve of Li-battery charging by 4 device units connected in series. Each SSF unit was dropped with 0.2 g water to charge the power storage devices.

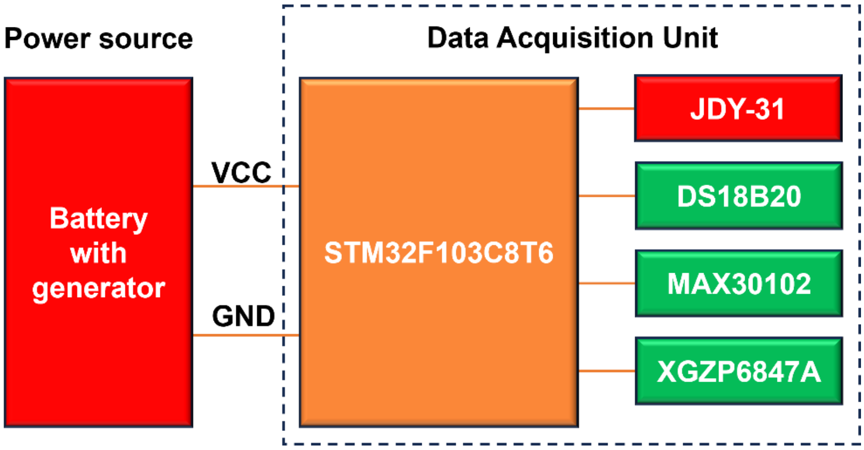

Supplementary Fig. 36 Block diagram illustrating the connection between the power source (battery charged by generator) and several key components of the acquisition system (micro control unit: STM32F103C8T6, temperature senor unit: DS18B20, blue tooth unit: JDY-31, heart rate sensor: MAX30102, pressure sensor: XGZP6847A).

References and Notes

1. Xue, G. B. *et al.* Water-evaporation-induced electricity with nanostructured carbon materials. *Nat. Nanotechnol.* **12**, 317–321 (2017).
2. Guo, C. Y. *et al.* Radiative cooling assisted self-sustaining and highly efficient moisture energy harvesting. *Nat. Commun.* **15**, 6100 (2024).
3. He, W. Y. *et al.* Textile-based moisture power generator with dual asymmetric structure and high flexibility for wearable applications. *Nano Energy* **95**, 107017 (2022).
4. Hu, Y. H. *et al.* Phyto-inspired sustainable and high-performance fabric generators via moisture absorption-evaporation cycles. *Sci. Adv.* **10**, eadk4620 (2024).
5. Zhao, K. Y. *et al.* Humidity-tolerant moisture-driven energy generator with Mxene aerogel-organohydrogel bilayer. *Acs Nano* **17**, 5472–5485 (2023).
6. Tan, J. *et al.* Self-sustained electricity generator driven by the compatible integration of ambient moisture adsorption and evaporation. *Nat. Commun.* **13**, 3643 (2022).
7. Wang, H. Y. *et al.* Bilayer of polyelectrolyte films for spontaneous power generation in air up to an integrated 1,000 V output. *Nat. Nanotechnol.* **16**, 811–819 (2021).
8. He, T. C. *et al.* Fully printed planar moisture-enabled electric generator arrays for scalable function integration. *Joule* **7**, 935–951 (2023).
9. Qin, Y. S. *et al.* Constant electricity generation in nanostructured silicon by evaporation-driven water flow. *Angew. Chem. Int. Edit.* **59**, 10619–10625 (2020).
10. Liu, X. M. *et al.* Power generation from ambient humidity using protein nanowires. *Nature* **578**, 550–554 (2020).
11. Shou, D. H., Fan, J. T. An all hydrophilic fluid diode for unidirectional flow in porous systems. *Adv. Funct. Mater.* **28**, 1800269 (2018).
12. Tao, P. *et al.* Solar-driven interfacial evaporation. *Nat. Energy* **3**, 1031–1041 (2018).
13. Zhou, X. Y., Zhao, F., Guo, Y. H., Rosenberger, B., Yu, G. H. Architecting highly hydratable polymer networks to tune the water state for solar water purification. *Sci. Adv.* **5**, eaaw5484 (2019).
14. He, X. B., Man, V. H., Yang, W., Lee, T. S., Wang, J. M. A fast and high-quality charge model for the next generation general amber force field. *J. Chem. Phys.* **153**, 114502 (2020).
15. Bayly, C. I., Cieplak, P., Cornell, W. D., Kollman, P. A. A well-behaved electrostatic potential based method using charge restraints for deriving atomic charges - the resp model. *J. Phys. Chem.* **97**, 10269–10280 (1993).
16. Doherty, B., Zhong, X., Gathiaka, S., Li, B., Acevedo, O. Revisiting opls force field parameters for ionic liquid simulations. *J. Chem. Theory. Comput.* **13**, 6131–6145 (2017).
17. Martínez, L., Andrade, R., Birgin, E. G., Martínez, J. M. Packmol: A package for building initial configurations for molecular dynamics simulations. *J. Comput. Chem.* **30**, 2157–2164 (2009).
18. Van der Spoel, D., Lindahl, E., Hess, B., Groenhof, G., Mark, A. E., Berendsen, H. J. C. Gromacs: Fast, flexible, and free. *J. Comput. Chem.* **26**, 1701–1718 (2005).
19. Yang, H. C. *et al.* Dissolution-precipitation dynamics in ester electrolyte for high-stability lithium metal batteries. *Acs Energy Lett.* **6**, 1413–1421 (2021).
20. Fu, J. L. *et al.* Lithium nitrate regulated sulfone electrolytes for lithium metal batteries. *Angew. Chem. Int. Edit.* **59**, 22194–22201 (2020).
21. Lu, T., Chen, F. W. Multiwfn: A multifunctional wavefunction analyzer. *J. Comput. Chem.* **33**, 580–592 (2012).
22. Humphrey, W., Dalke, A., Schulten, K. Vmd: Visual molecular dynamics. *J. Mol. Graph. Model.* **14**, 33–38 (1996).
23. Stephens, P. J., Devlin, F. J., Chabalowski, C. F., Frisch, M. J. Ab-initio calculation of vibrational absorption and circular-dichroism spectra using density-functional force-fields. *J. Phys. Chem.* **98**, 11623–11627 (1994).
24. Grimme, S., Antony, J., Ehrlich, S., Krieg, H. A consistent and accurate ab initio parametrization of density functional dispersion correction (dft-d) for the 94 elements h-pu. *J. Chem. Phys.* **132**, 154104 (2010).
25. Zhao, Y., Truhlar, D. G. The m06 suite of density functionals for main group thermochemistry, thermochemical kinetics, noncovalent interactions, excited states, and transition elements: Two

new functionals and systematic testing of four m06-class functionals and 12 other functionals. *Theor. Chem. Acc.* **120**, 215–241 (2008).

26. Xiong, X. G., Sugiura, A., Yanai, T. Projector augmented wave method with gauss-type atomic orbital basis: Implementation of the generalized gradient approximation and mesh grid quadrature. *J. Chem. Theory. Comput.* **16**, 4883–4898 (2020).
27. Ramakrishnan, K., Das, S., Motamarri, P. Fast and scalable finite-element based approach for density functional theory calculations using projector augmented wave method. *Phys. Rev. B* **111**, 035101 (2025).
28. Perdew, J. P., Burke, K., Ernzerhof, M. Generalized gradient approximation made simple. *Phys. Rev. Lett.* **77**, 3865–3868 (1996).
29. Chen, S. Y., Salzbrenner, P. T., Monserrat, B. Nonuniform grids for brillouin zone integration and interpolation. *Phys. Rev. B* **106**, 155102 (2022).
30. Henkelman, G., Uberuaga, B. P., Jónsson, H. A climbing image nudged elastic band method for finding saddle points and minimum energy paths. *J. Chem. Phys.* **113**, 9901–9904 (2000).